
Proton Core Imaging of the Nuclear Burn in Inertial Confinement Fusion Implosions

Introduction

Images of the nuclear burn region in inertial confinement fusion (ICF)^{1,2} experiments can provide critical information about the complex dynamics of fuel capsule implosions, showing the spatial distributions of nuclear reactions that result from the cumulative effects of drive and compression including fuel–shell mix, implosion asymmetries, and radiation and heat transport. Such image data provide exacting tests for simulations. Burn images of deuterium–tritium-filled capsules have previously been envisioned³ and made using 14.1-MeV neutrons,^{4–7} 3-MeV protons,^{8–10} or 3.5-MeV alpha particles¹⁰ (see other papers cited in Ref. 11).

This article is the second in a series that discusses another burn imaging method based on the energetic 14.7-MeV protons from reactions in fuel with deuterium (D) and 3-helium (³He) ions. This method, utilizing multiple proton-emission cameras, allows us to study the sizes and asymmetries of burn regions in a wide range of imploded thick plastic-shell capsules that are not amenable to imaging with lower-energy charged particles (which cannot penetrate the shell) and with more angular views than have been obtained so far with neutron imaging. The first article¹¹ described the general method, presented mathematical algorithms used, and evaluated the spatial resolution and signal-to-noise issues. Here we describe details of the imaging hardware, a sample analysis of a radial burn profile measurement, and experiments and calculations that have been performed to test the accuracy of the measurements. In future articles we will show more details about analysis algorithms,¹² systematic studies of the effects of capsule and drive conditions on burn region size for a large number of nominally symmetric implosions,^{12,13} and the effects of drive asymmetry and capsule-shell asymmetry on implosion asymmetry.¹⁴

The proton-emission imaging cameras generate penumbral images of the burn region that are deconvolved using techniques described in Refs. 11 and 12. Two separate approaches are utilized; one generates a 2-D surface-brightness image of the burn, while the other generates a radial burn profile (reactions

per unit volume) for nominally symmetric implosions. The work described here uses only the second approach.

The structure of this paper is as follows. **Hardware and Design Features** (p. 196) describes the camera hardware, which consists primarily of an imaging aperture and a detector pack utilizing CR-39 solid-state nuclear track detectors. **Sample Data From a Capsule With a Plastic Shell** (p. 199) shows sample raw experimental data obtained from an implosion along with the corresponding deconvolved radial profile of emissivity in the imploded capsule. **Demonstration That Possible Sources of Image Broadening are Unimportant** (p. 200) investigates four possible sources of image degradation, all of which are shown to be unimportant. **Fidelity of the Measured Burn Region Sizes** (p. 204) discusses several experimental demonstrations of the fidelity of the reconstructed images, and **Discussion** (p. 205) summarizes the main results.

Hardware and Design Features

Three identical proton core imaging system (PCIS) cameras have been fabricated and used simultaneously for imaging D³He burn from three (nearly) orthogonal directions at the OMEGA Laser Facility.¹⁵ Design criteria for individual cameras included flexibility in imaging geometry and detector filter assignments for imaging of various implosion types, modularized design for simplified installation and minimization of turn-around time between successive experiments, and a redundant “dual detection” scheme for verifying results and backup in case of defective detectors.

The integrated system has proven very effective and practical for obtaining burn images at OMEGA. Figure 104.37 shows a schematic of three proton-emission imaging cameras mounted on the OMEGA target chamber, where each camera is positioned by a special diagnostic shuttle system. The simultaneous use of three cameras makes possible studies of burn symmetry^{11,14} and camera consistency [see **Fidelity of the Measured Burn Region Sizes** (p. 204)]. The structure of an individual camera is shown in Fig. 104.38.

After leaving an imploded capsule, protons pass through a round aperture before striking a detector pack. The aperture is typically a 2000- μm -diam hole machined into a 500- μm -thick tantalum (Ta) substrate, although diameters as small as 500 μm have occasionally been used. An accurate, clean, and burr-free

edge for the aperture wall is obtained using electrodischarge machining. Each aperture is inspected and quantitatively characterized on both sides using a microscope with a calibrated X-Y stage and a high-resolution camera to determine that deviations from roundness are small; going around the circumference, the rms deviation from constant radius is not allowed to exceed 3 μm and is usually considerably smaller.

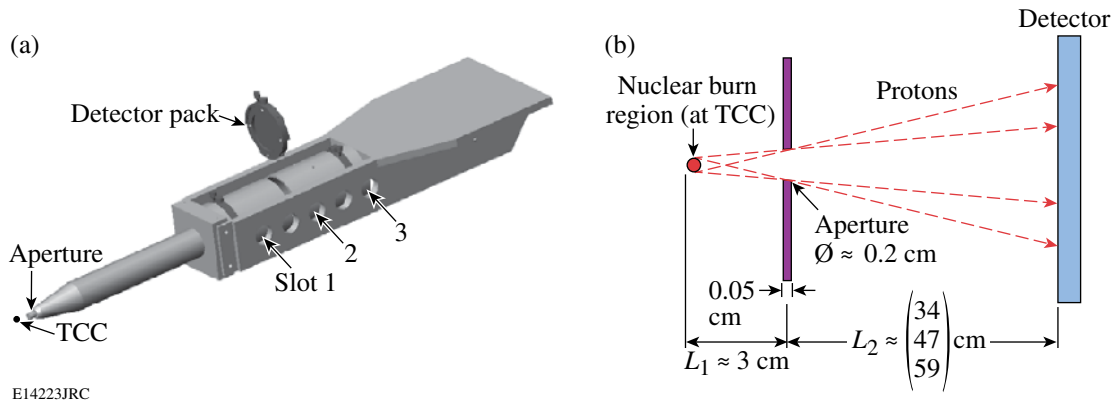


E14222JRC

Figure 104.37 Schematic of the OMEGA target chamber with three cameras for imaging a capsule implosion. The capsule is positioned at target chamber center by the positioning system located at 11 o'clock. The three structures at 1, 4, and 5 o'clock are the PCIS cameras, located approximately orthogonal to each other. This orthogonality is especially important for probing asymmetric burn.

The distance of the aperture from the imploded capsule, which is located at target chamber center (TCC), is usually as small as possible (~3 cm) to maximize counting statistics;¹¹ closer placement is not possible without interfering with laser beams. The region between the aperture and the detector is enclosed within a conductive housing [Fig. 104.38(a)]. This enclosure prevents stray charged particles from reaching the detectors and shields signal protons from possible electric and magnetic fields.

The detector pack consists of a layered assembly of metallic foils and CR-39 detectors¹⁶ held in an aluminum (Al) support. The metallic foils act as ranging filters for reducing the energy of incoming protons to the energy range 0.5 to 8 MeV, where CR-39 proton detection efficiency is essentially 100%. After exposure, each detector is etched in NaOH and scanned on an automated microscope system that locates the track of each incident proton to submicron accuracy. The distribution of proton track density on the detector forms the penumbral image referred to above.



E14223JRC

Figure 104.38 (a) Illustration of the proton-emission imaging hardware. The capsule implosion is located at target chamber center (TCC), which is about 3 cm from the imaging aperture. A detector pack may be positioned in one of three available slots (34, 47, and 59 cm from the aperture), providing geometric magnification of the capsule structure ($M \equiv L_2/L_1$) of 12.5, 16, or 20. The aperture consists of a 0.2-cm hole in a 500- μm -thick tantalum substrate. The total length of the instrument is 93 cm. (b) A line diagram illustrates the dimensions.

The choice of filters depends on the expected proton spectrum, which can be different for different types of capsule implosions. Figure 104.39 shows spectra for a 20- μm -thick plastic-shell capsule and a 2- μm -thick glass-shell capsule, which had mean proton energies of 13 MeV and 14.5 MeV, respectively. The plastic-shell implosion might be imaged using a single 800- μm -thick Al filter, while the glass-shell implosion might require a 1000- μm filter. Rather than a single filter, a

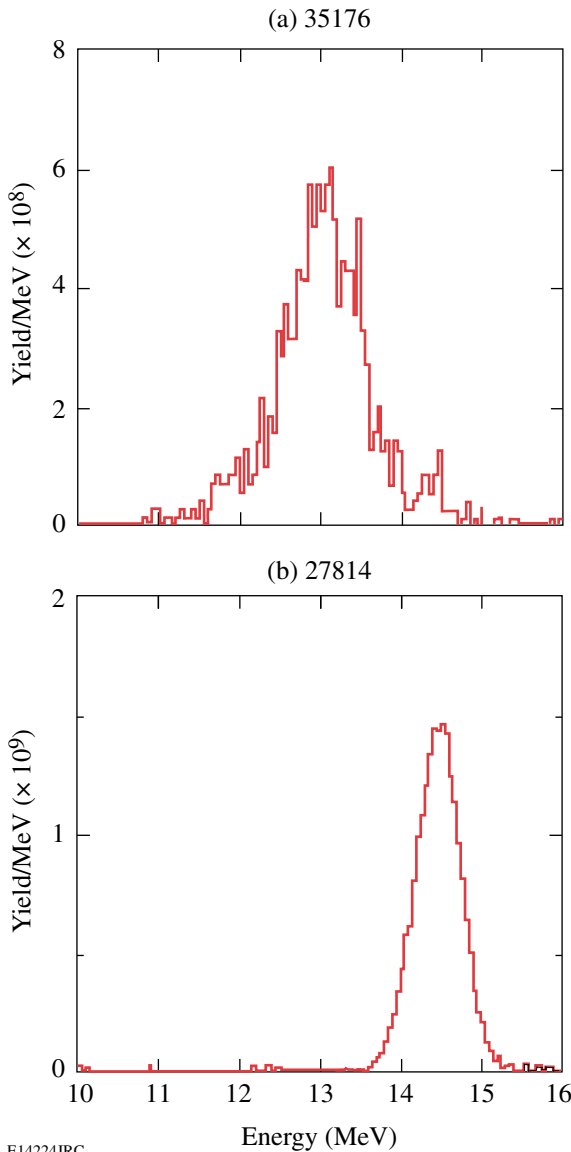


Figure 104.39 For proton-emission imaging, filters are used to reduce the incident proton energies to the range 0.5–8 MeV, where the CR-39 detectors are 100% efficient. Different implosion types result in somewhat different proton energies, as shown here, and filters must be chosen accordingly. (a) A 20- μm -thick CH capsule (shot 35176). (b) A 2.3- μm glass capsule (shot 27814).

series of filters and sheets of CR-39 are usually stacked to provide two redundant images from a single camera. As illustrated in Fig. 104.40(a), two images of the D^3He burn are obtained when a thick filter is placed in front of two back-to-back sheets of CR-39. The filter and first sheet of CR-39 range down the energetic D^3He protons for optimal detection on the back of the first sheet and again on the front of the second sheet. The redundant data are occasionally useful if one CR-39 detector has any defects (such as anomalous intrinsic noise¹⁶). Figure 104.40(b) illustrates another filter configuration that can be used for redundant data. This one places a thin filter between the two pieces of CR-39 so that the proton energy is slightly different at the two detector surfaces. This can be useful if there is a significant uncertainty in what the proton energy will be or if the proton spectrum is particularly wide; if the spectrum at the first sheet is not optimum for detection, the spectrum at the other sheet may be better.

The distance from the aperture to the detector pack can be varied by positioning the detector in any of three designated slots [shown in Fig. 104.38(a)]. The first slot provides a nominal 12.5 \times geometric magnification M (the ratio L_2/L_1), the second

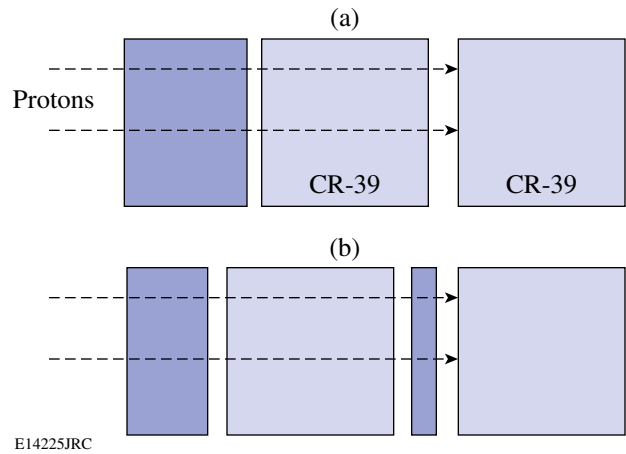


Figure 104.40 Two examples of how CR-39 detectors and filters can be stacked for redundant “front-back” particle detection. (a) Protons lose enough energy while passing through the filter and the first piece of CR-39 so that their energies are in the range of 100% detection efficiency and they leave tracks on both the back side of the first piece and the front side of the second piece. This provides protection against the possibility that either detector has a defect. (b) Protons lose enough energy while passing through the first filter and the first piece of CR-39 so that they leave tracks on the back side of the first piece. They lose slightly more energy while passing through another thin filter, leaving tracks on the front side of the second piece. This provides some protection against the possibility that the proton energy was too low at the second piece; the higher energy at the back of the first piece may then be optimal.

provides $16\times$, and the third provides $20\times$. The position is usually chosen to optimize the density of proton tracks on the detectors, which begin to saturate if the incident proton density exceeds $\sim 10^6$ protons/cm². The third slot makes possible the formation of images for D³He yields up to $\sim 5 \times 10^{10}$.

Each camera is secured to a ten-inch manipulator (TIM) on the OMEGA target chamber by way of the large, flat structure at the back end of the system (Fig. 104.38). The TIM's are diagnostic shuttle systems used to position diagnostics near the implosion. There are six TIM's on the OMEGA target chamber, allowing for the use of multiple PCIS cameras. The TIM's facilitate the installation, positioning, and removal of the cameras. Ease of access is essential since the aperture and detector pack of each camera must be replaced between every laser shot. Modularized aperture and detector packs have been implemented to ensure that the replacement time does not exceed the typical shot-to-shot time interval of the OMEGA laser.

Sample Data From a Capsule With a Plastic Shell

The proton-emission imaging cameras have been used to examine many implosions at the OMEGA Laser System; the majority of these involved direct illumination of warm plastic-shell capsules filled with a D³He gas mixture. These capsules were usually driven by 60 beams of frequency-tripled ($0.35\text{-}\mu\text{m}$) UV light, with total laser energy of 23 kJ delivered in a 1-ns square pulse.¹⁷ Individual beams underwent 1.0-THz 2-D smoothing by spectral dispersion and polarization smoothing applied through the use of birefringent wedges.¹⁸

Structural information about the source of protons in an experiment is obtained by deconvolving a penumbral-camera image using the method described in Ref. 11 and expanded in Ref. 12, which gives the time-integrated radial burn profile (reactions per μm^3) in the implosion. First the azimuthally averaged proton density $N(R)$ in the penumbral image is used to calculate the radial derivative dN/dR , as illustrated in Fig. 104.41. An example using real data is shown in Fig. 104.42(a) (from OMEGA implosion 36730, with 18-atm D³He in a $17\text{-}\mu\text{m}$ -thick plastic shell). This derivative is then fit with a family of functions of varying shapes that are analytically or numerically related to functions describing the radial profile $S_{\text{burn}}(r)$ of proton emissivity per unit volume. The result is a determination of the shape and the characteristic size of the burn region itself. The size can be quantified in different ways, but the radius R_{burn} containing 1/2 of the total local emission seems quite independent of the emission profile shape (as discussed in Ref. 12) and will be used here. For local emission profile shapes we can use the family of super-Gaussians

$$S_{\text{burn}}(r) = S_0 \exp\left[-(r/r_0)^{2/p}\right], \quad (1)$$

where p is a “peakedness” shape parameter and $r_0 = r_0(R_{\text{burn}}, p)$ is a radius. Numerically converting $S_{\text{burn}}(r)$ to functions for comparison with dN/dR , we find the best fit illustrated in Fig. 104.42(a); the corresponding radial profile of emissivity in the capsule is shown in Fig. 104.42(b) and has $R_{\text{burn}} = 32 \mu\text{m}$. To give an idea of statistical errors, Fig. 104.42(b) shows inferred local emission profiles corresponding to alternative fits to the raw data with total χ^2 value higher than the minimum by one. The uncertainty in the shape is significant, but the uncertainty in R_{burn} is only about $1.6 \mu\text{m}$ (see Ref. 12 for discussion). Note that the analysis produces absolutely normalized emissivity values.

The D³He burn data from many nominally symmetric implosions have been characterized in this way. A range of R_{burn} values from 20 to $80 \mu\text{m}$ has been measured in other experiments, demonstrating the applicability of this imaging technique to widely different implosion types. The dependence of R_{burn} on implosion type is discussed in Ref. 12.

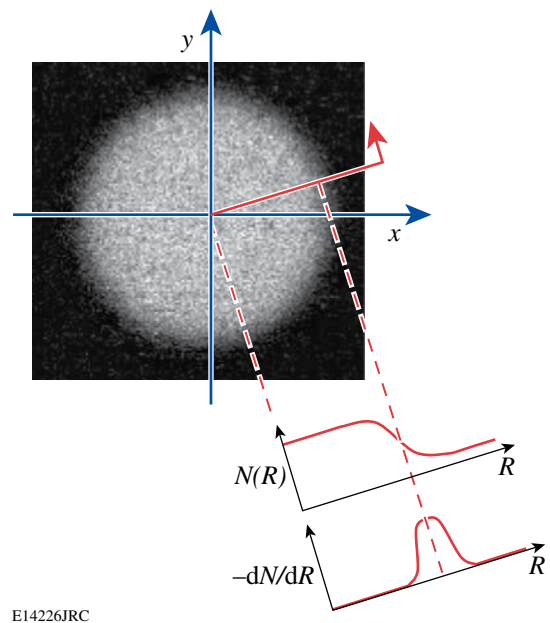
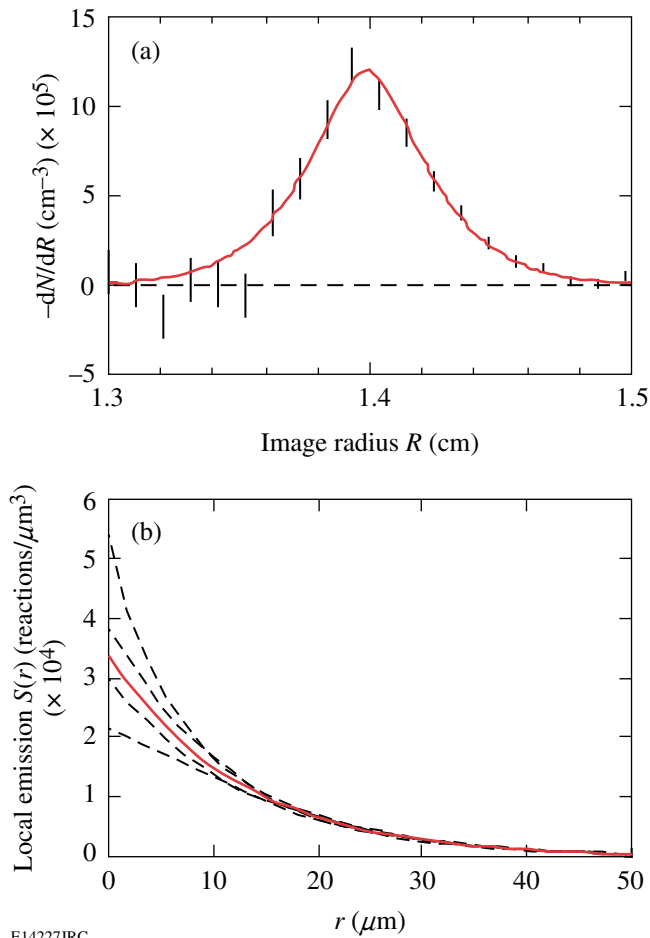


Figure 104.41
Illustration of the relationship between a raw penumbral image (brightness is proportional to the number of protons N per unit area on the detector) and its radial derivative. In the method implemented here, only the azimuthal average of this derivative is used. In the more general case, where asymmetric burn regions are studied, the angular variation of the radial derivative is used.¹¹



E14227JRC

Figure 104.42

(a) The radial derivative of the azimuthally averaged detected proton density (dN/dR) as a function of detector radius for OMEGA implosion 36730. The data were obtained with one of three proton-emission imaging cameras, and the implosion involved a 17- μm plastic shell with an 18-atm D^3He -gas fill. The statistical error bars are larger (smaller) toward the left (right) of the peak where dN/dR represents a small difference between two large (small) numbers. The solid line, representing the best fit to the data, corresponds to the radial burn profile (D^3He reactions per unit volume) shown in (b) with $R_{\text{burn}} = 32 \mu\text{m}$. The error envelope shown by the dashed lines in (b) was generated by using alternate fits to the raw data with χ^2 values exceeding χ^2_{min} by 1. Although the uncertainty in the shape is significant, the uncertainty in R_{burn} is only $\pm 1.6 \mu\text{m}$.

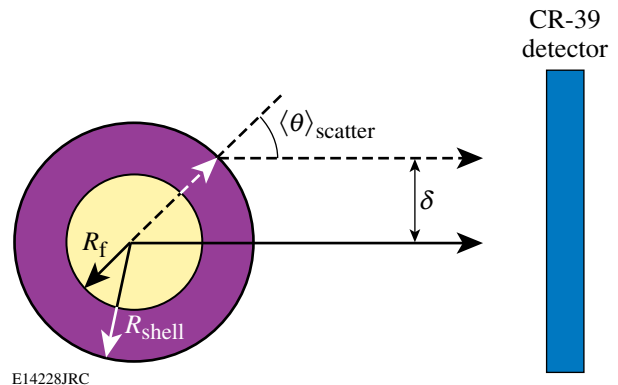
Demonstration that Possible Sources of Image Broadening are Unimportant

As illustrated in **Sample Data From a Capsule With a Plastic Shell** (p. 199), statistical errors in the measurement of burn region size are typically a few microns. In this section we investigate other possible sources of error. The protons that generate a penumbral image may experience trajectory shifts while traversing electric and magnetic fields and while interacting with different materials such as the capsule shell, aperture

substrate, and ranging filters. If these trajectory shifts are severe enough, the spatial structure in the penumbral image may be artificially broadened; the structure in deconvolved burn images or radial burn profiles will therefore also be broadened. The azimuthal average of the penumbra can also be broadened if the aperture is not round, and errors in analysis can occur from use of incorrect geometric parameters. If broadening with a characteristic length l occurs in the penumbral image, the deconvolved image of a point source (the point response function prf) will have a characteristic size l/M , where M is the geometric magnification of the camera (the value 12.5 is used in the following calculations). The effects of trajectory shifts are discussed in order of occurrence, beginning at the location of D^3He proton production and ending at the detector, and are followed by a consideration of errors in system geometry.

1. Scattering in the Compressed Capsule

The first significant materials encountered by the protons are the remnants of the shell that surround and compress the heated fuel region (see Fig. 104.43). Since the majority of implosions imaged with PCIS involved 20- μm -thick CH-plastic shells, this type of capsule will be examined. At the time of peak proton production, the shell material remaining after the ablation phase consists of a highly dense ($\sim 20 \text{ g/cc}$), low-temperature ($\sim 500\text{-eV}$) plasma.^{19,20} Spectral analysis



E14228JRC

Figure 104.43

illustration of the assumed geometry for estimating the degree of proton scattering in shell material. The radius of the fuel region R_f was taken to be $45 \mu\text{m}$; the outer radius of the shell R_{shell} was $80 \mu\text{m}$. Two proton paths originating from a point source are illustrated. The solid line represents the path taken by unscattered protons; the dashed line represents the worst-case path of scattered protons. The average scattering angle $\langle \theta \rangle_{\text{scatter}}$ was estimated both for cold CH and for a fully ionized CH plasma shell. The results were $\sim 1^\circ$ and 2° , respectively, producing corresponding source broadening δ of $\sim 1 \mu\text{m}$ and $3 \mu\text{m}$. Both are negligible compared to typical measured burn radii of $\sim 30 \mu\text{m}$.

of D^3He fusion protons has shown that the shell material, with a corresponding ρR of $\sim 60 \text{ mg/cm}^2$, is responsible for a downshift of a couple mega-electron volts from the 14.7-MeV birth energy [Fig. 104.39(a)].^{21,22} Although proton slowing down is associated with drag of the background electrons, a small amount of scattering will occur off background ions. To estimate the amount of this scattering and its effect on the broadening of the *prf* of the imaging system, two separate calculations were performed.

In the first calculation, the shell material was treated as a cold, dense solid. The Monte Carlo code TRIM²³ was used to simulate the slowing down and scatter of 14.7-MeV protons in the cold-shell material. The shell was treated as a 50/50 atomic mixture of carbon and hydrogen with a density of 20 g/cc and a thickness of 35 μm (a ρR of 70 mg/cm^2). The calculated average transmitted energy was 12.2 MeV, in reasonable agreement with experimental observations [Fig. 104.39(a)]. The average scattering angle was found to be 0.9° . Assuming the fuel-shell interface is at a radius of 45 μm and all scattering occurs on the outside edge of the shell, a worst-case amount of apparent source broadening was estimated to be $\sim 1 \mu\text{m}$ (see Fig. 104.43).

In the second, more realistic calculation, the compressed shell material was treated as hot plasma at a temperature of 500 eV.^{19,20} At this temperature and density, the shell atoms are fully ionized.²⁴ With minor modifications to Rutherford's scattering formula,²⁵ the mean squared angle of the scattered particles is given by

$$\langle \theta^2 \rangle \cong 2\pi N_i (2zeZe/pv)^2 (\ln \Lambda)t, \quad (2)$$

where N_i is the ion species density in the background plasma; t is the shell thickness; Ze is the charge of the scattering material; ze is the charge of the incident particle, with momentum p , and speed v ; and $\ln \Lambda$ is the Coulomb logarithm. The mean scattering angle was calculated for 12-MeV protons passing through 35 μm of a 500-eV, 20-g/cc CH plasma with a Coulomb logarithm of approximately 13.^{19,20} (An initial energy of 12 MeV and a ρR of 70 mg/cm^2 were selected to overestimate the effect.) The calculations gave an average scatter angle of $\sim 2^\circ$, corresponding to a broadening of the *prf* by $\sim 3 \mu\text{m}$. (A similar calculation was performed for scattering in the fuel region, but the effect was much smaller.)

2. Trajectory Shifts Due to Electric Fields

During the laser pulse of a direct-drive implosion, hot electrons are blown off the capsule and may redeposit themselves

on surrounding structures, temporarily establishing electric fields. The purpose of this section is to examine the effect a potential difference between the capsule and the aperture could have on proton trajectories and ultimately on the *prf* of the instrument. Although the effect is complicated by the structure of the OMEGA target chamber and the dynamics of the implosion, these calculations look at simplified geometries to produce an order of magnitude estimate of the effect.

A program was developed for tracking the trajectories of 14.7-MeV protons emitted from a point source as they pass through a negatively charged aperture substrate and on to the CR-39 detector plane. A diagram of the geometry is shown in Fig. 104.44(a). The aperture was positioned 3.3 cm from the

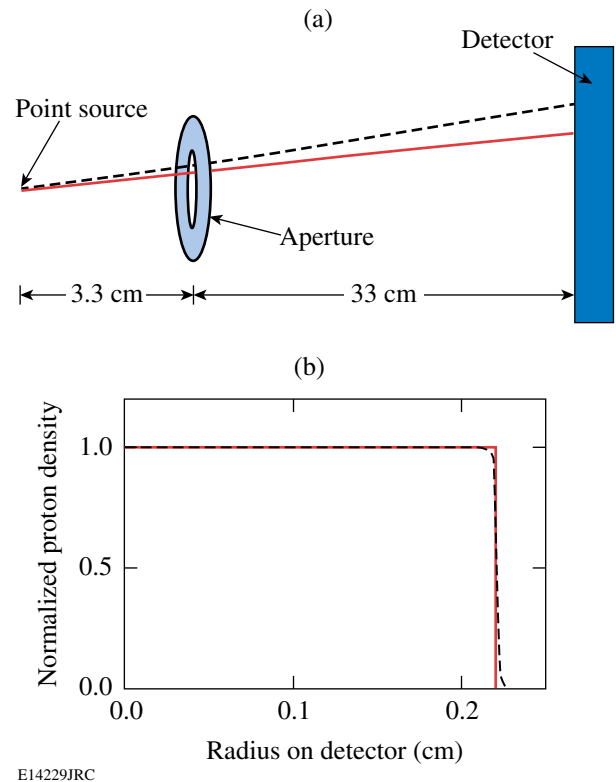


Figure 104.44

(a) Illustration of the effect of electric fields on proton trajectories. The dashed line schematically represents the proton path when a 200- μm -radius aperture carries a potential of 1 MV relative to the source (an overestimate of realistic conditions), while the solid line represents the proton path when no potential is present. Calculations were performed to estimate the image broadening of a point source. (b) The simulated proton density striking the detector for the case of no potential (solid line) and 1-MV potential (dashed line). The result was a slight outward shift of the image and a broadening of the point source by $\sim 1 \mu\text{m}$. This broadening is small compared to a typical burn radius of $\sim 30 \mu\text{m}$.

source, and the detector plane was positioned an additional 33 cm past the aperture. The figure illustrates one possible effect of a charged aperture where a proton path is indicated for two scenarios: for the case of a charged aperture (dashed line) and the case of an uncharged aperture (solid line).

The aperture substrate was modeled by a 1-cm-radius disk carrying a uniform negative charge corresponding to a potential between the source and this disk of 1 MV. The magnitude of the potential was chosen to overestimate the experimental values expected. Experiments indicate that the capsule itself may carry a charge of approximately 1 MV during the laser pulse, but that the potential quickly dissipates once the laser pulse is terminated.^{26,27} For the PCIS experiments, the proton production occurs several hundred picoseconds after laser pulse is terminated, providing a significant period of time in which the potential is known to have substantially decayed.

Calculations were performed for a 200- μm -radius aperture located in the center of the 1-cm-radius disk. Protons were launched through the aperture in all allowable directions. The code calculated particle forces and trajectories on a time scale corresponding to a 5- μm step in the linear dimension using a standard integration for the velocity and a second-order Runge–Kutta integration for the radial position. Simulations were performed with the electric field symmetric on both sides of the aperture as well as with the field turned off between the aperture and the detector, modeling the limit of a perfectly conductive cavity enclosing the instrument. Particle trajectories were individually tracked and particle-particle interactions were not included, as the particle density in the experiments is small. The simulated proton density striking the detector is shown in Fig. 104.44(b) for the case of symmetric fields. The solid line represents the proton density when no net potential exists between the source and the aperture, and the dashed line represents the proton density for a 1-MV potential.

The purpose of this study was to estimate the effect of a potential difference between the aperture and the capsule on the *prf* of the camera. For both symmetric and asymmetric fields, the *prf* was found to be broadened by only $\sim 1 \mu\text{m}$. (Additional simulations were also performed for a 500- μm -radius aperture, as well as for a 0.1-MV potential. None of the studies produced a significant broadening of the image.)

3. Scattering in Aperture Walls

One advantage of proton-emission imaging is that a thin aperture substrate is sufficient to stop D^3He protons, providing a well-defined aperture edge. The apertures commonly used

consist of a 2000- μm -diam cylindrical hole in a 500- μm -thick Ta substrate. The 14.7-MeV protons would be completely stopped by $\sim 400 \mu\text{m}$ of Ta. Protons that travel through less Ta may be stopped in the ranging filters located in the detector pack. Ideally, no detected protons would have scattered in the Ta. Since no aperture is perfectly tapered to match the trajectories of incoming protons, however, some protons will strike the inner walls of the aperture and scatter through a thinner section of Ta, as illustrated in Fig. 104.45(a). If the

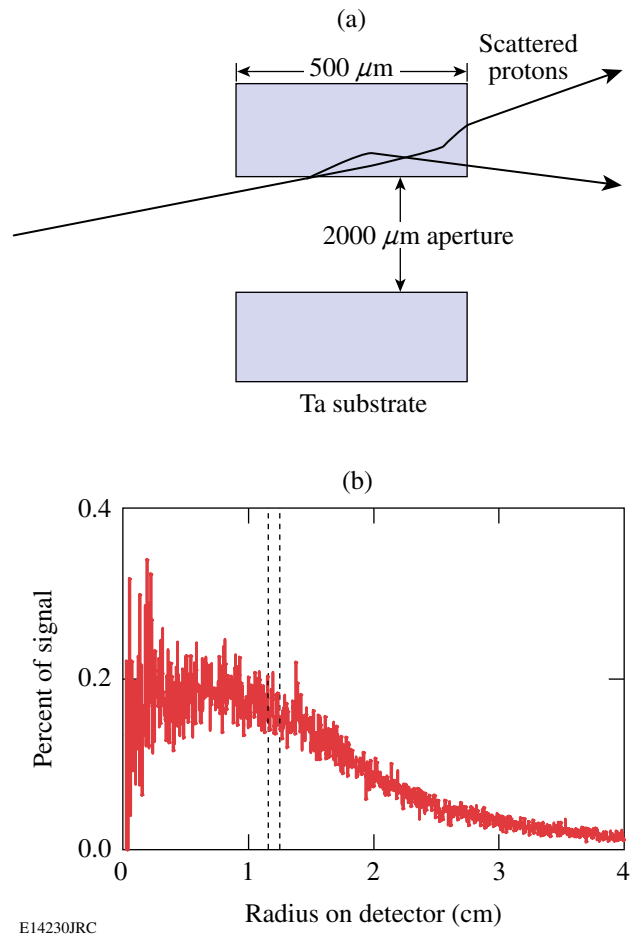


Figure 104.45

(a) Illustration of a cross sectional view of an aperture, defined as a 2000- μm -diam hole in a 500- μm -thick tantalum substrate. Not shown are the source and the detector, located 3 cm to the left and 33 cm to the right, respectively. As seen in the figure, the geometry dictates that protons may encounter less than 500 μm of Ta. If the amount of Ta encountered is sufficiently small, the protons will exit the tantalum and may broaden the image. (b) The simulated ratio of scattered proton density to unscattered signal proton density on the detector. The dotted lines represent the approximate location of an image penumbra from an $\sim 30 \mu\text{m}$ source. The calculated broadening of the point source was $\ll 1 \mu\text{m}$.

section is thin enough, protons may exit the opposite side, travel to the detector pack, pass through the ranging filters, and be detected on the CR-39. The result would be a slight broadening of the penumbra.

Simulations were performed to estimate the degradation of the camera *prf* by proton scattering in the Ta substrate utilizing the Monte Carlo program TRIM²³ to evaluate the slowing down and scatter of charged particles in matter. The source was treated as a 12-MeV monoenergetic point source of protons, chosen to approximate the observed mean energy of D³He protons after escaping an imploded 20- μ m CH-shell capsule. TRIM was used to determine the amount of scatter produced by discrete thicknesses of Ta; since the aperture wall presents a continuous range of thicknesses to protons, some assumptions were made to transform the 1-D TRIM output into the 2-D geometry of the aperture. Instead of modeling the continuous range of thicknesses, a series of seven discrete thickness steps was used. Depending on where the proton entered the aperture wall, the encountered material was approximated by one of seven Ta sheets, ranging in thickness from 10 μ m to 150 μ m. (Any proton passing through more than 150 μ m of Ta would be stopped by the ranging filters.) Several million protons were tracked through each discrete thickness. Upon exiting the Ta material, the energy and trajectory of each proton was recorded.

These trajectories, along with the system geometry, were used to predict whether scattered protons would strike the detector plane. The system geometry mimicked the actual experimental hardware; modeling of the three main components, the source, the aperture, and the detector was included. The geometry was similar to that seen in Fig. 104.38(b), where the distance from TCC to the aperture was taken to be 3 cm and the distance from the aperture to the detector was 33 cm. The aperture was modeled by a 2000- μ m-diam hole centered in a 500- μ m-thick Ta disk. Based on this geometry and the recorded trajectories from TRIM, the scattered protons that reached the detector pack were isolated from those that did not.

Each proton deflected toward the detector pack then encountered additional filtering before reaching the detector. The filtering, placed directly in front of the detector, was assumed to be 20 μ m of Al followed by 1000 μ m of Mylar and an additional 100 μ m of Al. (Mylar has chemical composition and stopping properties similar to those of CR-39). The proton was assumed detected if the energy was great enough to allow passage through these additional filters.

Thus, a record of the detection locations of all the scattered protons with an appropriate trajectory and energy was created. The ratio of the scattered proton density to unscattered signal proton density as a function of the detector radius is shown in Fig. 104.45(b); the dotted lines indicate the approximate location of the image penumbra from an \sim 30- μ m source. The simulations showed that the scattered protons represent less than 0.3% of the detected protons in the penumbral region and that the radial profile of scattered protons is fairly flat. Since the radial derivative of the proton density ultimately determines the size and shape of the source,¹¹ the small-amplitude slowly varying background would have little effect. Broadening of the *prf* was found to be \ll 1 μ m.

4. Scattering in Filters

Upon reaching the detector pack, protons pass through several ranging filters that are designed to reduce the incident proton energy for optimal detection efficiency. Along with the desired loss of energy, the protons will experience some lateral straggling, another possible source of spatial broadening. To estimate the magnitude of this effect, the Monte Carlo code TRIM was used to track 12-MeV protons from a point source through 20 μ m of Al, 1000 μ m of Mylar, and a final 100 μ m of Al. The lateral positions for protons exiting the filters were recorded and fit by a Gaussian distribution with an *e*-folding radius at the detector of \sim 30 μ m. This translates to a broadening in the camera *prf* of \sim 30 μ m/*M* \sim 3 μ m.

5. Geometric Error

Accuracy in the inference of burn profiles from penumbral images requires accurate knowledge of imaging system dimensions. Of primary importance is the radius of the aperture projection on the detector, which may not be exactly as expected if either the capsule–aperture distance or the aperture–detector distance has any uncertainty. But the radius is actually determined from the data as an integral part of the analysis [see Refs. 11 and 12 and Fig. 104.42(a)], so this is not a source of error beyond the statistical fit error. If the aperture itself is not perfectly round and has deviations from its average radius with the rms value $\delta R_{\text{aperture}}$, the rms deviation from round at the detector will be $(M+1) \delta R_{\text{aperture}}$; this will cause a broadening of the system *prf* by $[(M+1)/M] \delta R_{\text{aperture}} \approx \delta R_{\text{aperture}}$. If the deviation from roundness is due to ellipticity, either from bad fabrication or from the aperture not being exactly perpendicular to the capsule–detector direction, this effect is identified in the data processing and corrected. Other types of deviation from roundness can sometimes be identi-

fied in the data, but in the worst case, uncorrected deviations should have $\delta R_{\text{aperture}} < 3 \mu\text{m}$ as discussed in **Hardware and Design Features** (p. 196).

Another source of error would come from an inaccurate value of the magnification M (see Fig. 104.38 and its caption), which could be different from the expected value if L_1 or L_2 were not measured accurately. Since M represents the ratio of structure size at the detector to structure size in the burn region, any error in M would not cause a broadening of the prf but would cause a multiplicative error in the inferred burn region size. But since the radius of the aperture itself, R_{aperture} , is measured in advance to better than 0.1%, and since the radius of its projection on the detector, $(M+1)R_{\text{aperture}}$, is determined as part of the data analysis, a self-consistent value of M is determined from the data and is not subject to measurement error.

6. Net Broadening

The net result of these broadening effects can be estimated for the data shown in Fig. 104.42 where the measured R_{burn} was found to be $32 \mu\text{m}$ with a statistical error of $\pm 1.6 \mu\text{m}$. If we assume that the five sources of error discussed in the previous subsections are independent and that each generates a distortion in the system prf that is approximately Gaussian, then the net system prf would be a Gaussian whose radius r_{prf} is the sum (in quadrature) of the individual radii. In this case, taking the upper limit for geometric error,

$$r_{prf} \approx \sqrt{3^2 + 1^2 + 0^2 + 3^2 + 3^2} \mu\text{m} \approx 5 \mu\text{m}.$$

The measured burn radius would then be the true burn radius added in quadrature with r_{prf} . The error would be

$$\begin{aligned} \delta R_{\text{burn}} &= R_{\text{burn,measured}} - R_{\text{burn,true}} \\ &\approx 32 \mu\text{m} - \sqrt{32^2 - 5^2} \mu\text{m} \approx 0.4 \mu\text{m}, \end{aligned} \quad (3)$$

which is small compared to the statistical uncertainty of $\pm 1.6 \mu\text{m}$.

Fidelity of the Measured Burn Region Sizes

The following subsections describe experimental tests that demonstrate the repeatability and fidelity of the measured burn region sizes. In **Consistency of the Measured Burn Profiles** (p. 204), measurement consistency is experimentally demon-

strated when six independent measurements of R_{burn} made during the same symmetrically driven implosion are compatible. **Lack of Dependence on Imaging Geometry** (p. 204) shows that the reconstructed burn profiles are independent of changes in the system magnification and the aperture size. **Lack of Distortion by Ambient Fields** (p. 205) presents data suggesting that ambient fields do not affect the system response.

1. Consistency of the Measured Burn Profiles

Figure 104.42(a) shows six separate measurements of R_{burn} made during the same symmetrically driven implosion (OMEGA shot 36730, a capsule with a $17\text{-}\mu\text{m}$ -thick plastic shell filled with a mixture of 6 atm of D_2 and 12 atm of ^3He gas). The implosion was imaged with three separate PCIS cameras, fielded in TIM's 2, 3, and 4. (TIM-3 is located 109° from TIM-2, and TIM-4 is 101° from TIM-2 and 79° from TIM-3.) Each camera produced two measurements of R_{burn} using the redundant detector method described in **Hardware and Design Features**. The error bars in the figure represent statistical uncertainties, as discussed in **Sample Data From a Capsule With a Plastic Shell** (p. 199), and the set of six measurements is self-consistent.

2. Lack of Dependence on Imaging Geometry

A measurement of R_{burn} should be independent of any changes in the geometric parameters of the camera, and this is demonstrated by data plotted in Fig. 104.46. Lack of dependence on aperture diameter is illustrated in Fig. 104.46(b), which shows results from five successive implosions of capsules with $19\text{-}\mu\text{m}$ -thick plastic shells filled with 10.5-atm D_2 and 6-atm ^3He . For each implosion, one TIM was equipped with a PCIS camera. The diameter of the aperture used for the first two and last two implosions was $2000 \mu\text{m}$, while the diameter used for the third implosion was $600 \mu\text{m}$. All results were statistically consistent with the mean value of $30 \mu\text{m}$. Lack of dependence on the geometric magnification was demonstrated by simultaneous use of cameras with different M on each of two implosions. In Fig. 104.46(a), data were taken with $M = 12.5$ and $M = 20$, while in Fig. 104.46(c) $M = 6$ and $M = 9$ were used. In each case the two different values of M resulted in the same measured R_{burn} .

3. Lack of Distortion by Ambient Fields

Several plastic-shell implosions were used to look for possible systematic errors associated with stray fields. The two cameras used for shot 35004 were set up identically except that $L_1 = 5.4 \text{ cm}$ for TIM-3 and $L_1 = 3.7 \text{ cm}$ for TIM-4. If fields were significantly influencing protons in the region between the capsule and the aperture, we would expect to see a difference

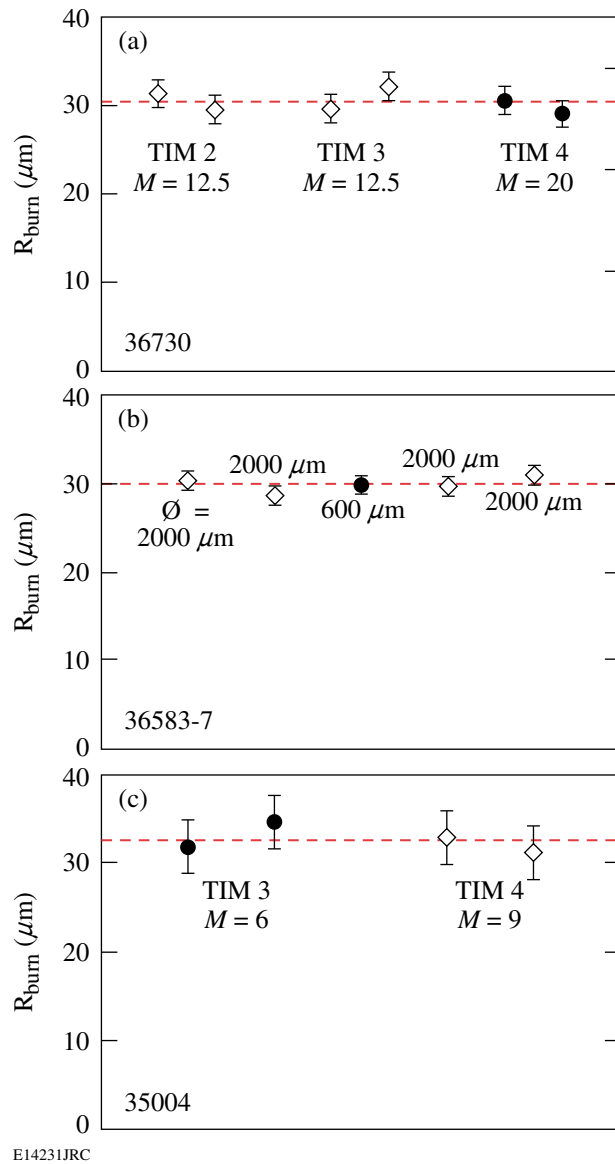


Figure 104.46

R_{burn} data are shown with the average measurement value (dashed line) for a series of implosions. (a) A $17\text{-}\mu\text{m}$ -thick plastic shell with 18-atm D^3He gas fill (OMEGA implosion 36730) was imaged by three nearly orthogonal imaging cameras with different aperture-to-detector distances, located in TIM's 2, 3, and 4. The redundant-detector method was used to generate two data sets for each camera. The geometric magnification (M) of each camera is listed. The data show that different cameras and different aperture-to-detector distances give the same result. (b) A single camera imaged a series of $19\text{-}\mu\text{m}$ -thick plastic shells filled with 10.5 atm D_2 and 6 atm ^3He . The aperture diameter (\emptyset) used for each camera is indicated; R_{burn} was unaffected by the change in aperture size. (c) A $20\text{-}\mu\text{m}$ -thick plastic shell with 18-atm D^3He gas fill was imaged by two cameras having different capsule-to-aperture distances, placed in TIM's 3 and 4. The separately inferred values of R_{burn} were statistically compatible. Note that the error bars in all plots are statistical errors.

in the measured R_{burn} from these two cameras. The results shown in Fig. 104.46(c) report essentially the same R_{burn} for both cameras, suggesting that there were no serious field effects in the region before the aperture.

The three cameras used for shot 36730 were set up identically except that $L_2 = 36.6\text{ cm}$ for TIM-2 and TIM-3 while $L_2 = 58.6\text{ cm}$ for TIM-4. If fields were affecting the protons between the aperture and the detector (a region surrounded by a conductor), we would expect to see differences in the measured values of R_{burn} . Figure 104.46(a) shows that all R_{burn} results were consistent, suggesting that there were no serious field effects in the region behind the aperture.

Another recent experiment²⁸ also provides evidence that fields do not dramatically alter the trajectory of D^3He protons in the region past the aperture. In this test, a steel mesh ($50\text{-}\mu\text{m}$ -diam wires with 100 wires per inch) was placed directly in front of the imaging aperture. Examination of the proton-emission image revealed no distortions in the mesh-induced pattern, suggesting that fields are not significantly altering the trajectories of 14.7-MeV D^3He protons.

Discussion

Three proton core imaging cameras have been built and installed at OMEGA using the design discussed here, and they have now been used to study the spatial distributions of nuclear burn in a range of different implosion types using algorithms described elsewhere.^{11,12} An example of the analysis of the radial burn profile of a symmetric implosion was shown in **Sample Data From a Capsule With a Plastic Shell** (p. 199) with a $32\text{-}\mu\text{m}$ burn radius. In another article,¹² other types of implosions are studied and are shown to have burn radii ranging from 20 to $80\text{ }\mu\text{m}$; clear correlations are shown between the burn radius and implosion parameters (capsule shell material and thickness, fill gas pressure, and laser energy). In addition, 2-D reconstruction techniques have been used together with three nearly orthogonal imaging cameras to study asymmetric burn regions and to show clear relationships between laser drive asymmetry and burn asymmetry.¹⁴ In Ref. 11 the issues of spatial resolution and statistical noise were studied theoretically. A range of calculations and measurements, described in **Demonstration that Possible Sources of Image Broadening are Unimportant** (p. 200) and **Fidelity of the Measured Burn Region Sizes** (p. 204), investigated other possible sources of error in measured burn region sizes. So far there is no evidence of any other errors that are as important as the statistical errors; more calculations and measurements as well as comparisons with x-ray and neutron images will be pursued in the future for

further verification. In the meantime, proton emission imaging is providing interesting and useful data bearing on the understanding of capsule implosion dynamics and performance. A particularly nice feature of this imaging mode, which will be utilized in future studies, is the fact that the same reaction product studied here (the D^3He proton) is also utilized by other diagnostics. Proton spectrometers¹⁶ measure the proton energy at different angles around a capsule, determining the areal density of the compressed shell from the energy loss, while the proton temporal diagnostic^{29,30} measures the time evolution of the burn. The spatial distribution of D^3He burn can therefore be combined with the angular distribution of areal density in the colder shell material and the time evolution of burn, as well as other types of diagnostic measurements, for a more complete picture of implosion dynamics.

ACKNOWLEDGEMENTS

The authors express their gratitude to the OMEGA engineers and operations crew who supported these experiments. In addition, we would like to personally thank Candice Culligan, and Jocelyn Schaeffer for their continuous help. This work has been supported in part by LLE (Subcontract No. P0410025G) and LLNL (Subcontract No. B313975), and by the U.S. Department of Energy Office of Inertial Confinement Fusion (Grant No. DE-FG03-99DP00300) and under Cooperative Agreement No. DE-FC03-92SF19460, the University of Rochester, and New York State Energy Research and Development Authority.

REFERENCES

1. J. Nuckolls *et al.*, *Nature* **239**, 139 (1972).
2. S. E. Bodner, D. G. Colombant, J. H. Gardner, R. H. Lehmborg, S. P. Obenschain, L. Phillips, A. J. Schmitt, J. D. Sethian, R. L. McCrory, W. Seka, C. P. Verdon, J. P. Knauer, B. B. Afeyan, and H. T. Powell, *Phys. Plasmas* **5**, 1901 (1998).
3. K. A. Nugent and B. Luther-Davies, *J. Appl. Phys.* **58**, 2508 (1985).
4. D. Ress *et al.*, *Rev. Sci. Instrum.* **59**, 1694 (1988).
5. R. A. Lerche *et al.*, *Laser Part. Beams* **9**, 99 (1991).
6. C. R. Christensen, D. C. Wilson, C. W. Barnes, G. P. Grim, G. L. Morgan, M. D. Wilke, F. J. Marshall, V. Yu. Glebov, and C. Stoeckl, *Phys. Plasmas* **11**, 2771 (2004).
7. L. Disdier, R. A. Lerche, J. L. Bourgade, and V. Yu. Glebov, *Rev. Sci. Instrum.* **75**, 2134 (2004).
8. Y.-W. Chen *et al.*, *Opt. Commun.* **73**, 337 (1989).
9. M. Nakai *et al.*, *Rev. Sci. Instrum.* **61**, 3235 (1990).
10. A. P. Fews *et al.*, *Phys. Rev. Lett.* **73**, 1801 (1994).
11. F. H. Séguin, J. L. DeCiantis, J. A. Frenje, S. Kurebayashi, C. K. Li, J. R. Rygg, C. Chen, V. Berube, B. E. Schwartz, R. D. Petrasso, V. A. Smalyuk, F. J. Marshall, J. P. Knauer, J. A. Delettrez, P. W. McKenty, D. D. Meyerhofer, S. Roberts, T. C. Sangster, K. Mikaelian, and H. S. Park, *Rev. Sci. Instrum.* **75**, 3520 (2004).
12. F. H. Séguin, J. L. DeCiantis, J. A. Frenje, C. K. Li, J. R. Rygg, C. D. Chen, R. D. Petrasso, J. A. Delettrez, S. P. Regan, V. A. Smalyuk, V. Yu. Glebov, J. P. Knauer, F. J. Marshall, D. D. Meyerhofer, S. Roberts, T. C. Sangster, C. Stoeckl, K. Mikaelian, H. S. Park, H. F. Robey, and R. E. Tipton, "Measured Dependence of Nuclear Burn Region Size on Implosion Parameters in Inertial Confinement Fusion Experiments," submitted to *Physics of Plasmas*.
13. J. L. DeCiantis, "Proton Emission Imaging of the Nuclear Burn in Inertial Confinement Fusion Experiments," M.S. thesis, Massachusetts Institute of Technology (2005).
14. F. H. Séguin, J. L. DeCiantis, J. A. Frenje, C. K. Li, J. R. Rygg, C. D. Chen, R. D. Petrasso, V. A. Smalyuk, F. J. Marshall, J. A. Delettrez, J. P. Knauer, P. W. McKenty, D. D. Meyerhofer, S. Roberts, T. C. Sangster, H. S. Mikaelian, and H. S. Park, *Bull. Am. Phys. Soc.* **49**, 63 (2004); F. H. Séguin, J. DeCiantis, C. K. Li, J. A. Frenje, J. R. Rygg, R. D. Petrasso, S. Regan, J. A. Delettrez, J. P. Knauer, F. J. Marshall, D. D. Meyerhofer, S. Roberts, T. C. Sangster, V. A. Smalyuk, H. S. Mikaelian, H. S. Park, H. Robey, and R. Tipton, *Bull. Am. Phys. Soc.* **50**, 114 (2005); *ibid.*, "Measured Effects of Drive Asymmetry and Shell Asymmetry on Nuclear Burn Region Symmetry in Direct-Drive ICF Implosions," to be submitted to *Physics of Plasmas*.
15. T. R. Boehly, D. L. Brown, R. S. Craxton, R. L. Keck, J. P. Knauer, J. H. Kelly, T. J. Kessler, S. A. Kumpan, S. J. Loucks, S. A. Letzring, F. J. Marshall, R. L. McCrory, S. F. B. Morse, W. Seka, J. M. Soures, and C. P. Verdon, *Opt. Commun.* **133**, 495 (1997).
16. F. H. Séguin, J. A. Frenje, C. K. Li, D. G. Hicks, S. Kurebayashi, J. R. Rygg, B.-E. Schwartz, R. D. Petrasso, S. Roberts, J. M. Soures, D. D. Meyerhofer, T. C. Sangster, J. P. Knauer, C. Sorce, V. Yu. Glebov, C. Stoeckl, T. W. Phillips, R. J. Leeper, K. Fletcher, and S. Padalino, *Rev. Sci. Instrum.* **74**, 975 (2003).
17. A series of burn images have been obtained from thin glass implosions involving less than 23 kJ of laser energy,¹² several thick plastic-shell implosions involving 18 kJ and 30 kJ of laser energy,^{12,14} and a few implosions involving different shaped laser pulses.¹³
18. T. R. Boehly, V. A. Smalyuk, D. D. Meyerhofer, J. P. Knauer, D. K. Bradley, R. S. Craxton, M. J. Guardalben, S. Skupsky, and T. J. Kessler, *J. Appl. Phys.* **85**, 3444 (1999).
19. C. Li and R. D. Petrasso, *Phys. Plasmas* **2**, 2460 (1995).
20. C. K. Li and R. D. Petrasso, *Phys. Rev. Lett.* **70**, 3059 (1993).
21. C. K. Li, D. G. Hicks, F. H. Séguin, J. A. Frenje, R. D. Petrasso, J. M. Soures, P. B. Radha, V. Yu. Glebov, C. Stoeckl, D. R. Harding, J. P. Knauer, R. L. Kremens, F. J. Marshall, D. D. Meyerhofer, S. Skupsky, S. Roberts, C. Sorce, T. C. Sangster, T. W. Phillips, M. D. Cable, and R. J. Leeper, *Phys. Plasmas* **7**, 2578 (2000).

22. F. H. Séguin, C. K. Li, J. A. Frenje, S. Kurebayashi, R. D. Petrasso, F. J. Marshall, D. D. Meyerhofer, J. M. Soures, T. C. Sangster, C. Stoeckl, J. A. Delettrez, P. B. Radha, V. A. Smalyuk, and S. Roberts, *Phys. Plasmas* **9**, 3558 (2002).
23. *SRIM*, a code for calculations of *The Stopping and Range of Ions in Matter*, J. F. Ziegler and J. P. Biersack, Version 2000.39 (2000).
24. D. E. Post *et al.*, *At. Data Nucl. Data Tables* **20**, 397 (1977).
25. J. D. Jackson, *Classical Electrodynamics*, 3rd ed. (Wiley, New York, 1999).
26. D. G. Hicks, C. K. Li, F. H. Séguin, J. D. Schnittman, A. K. Ram, J. A. Frenje, R. D. Petrasso, J. M. Soures, D. D. Meyerhofer, S. Roberts, C. Sorce, C. Stoeckl, T. C. Sangster, and T. W. Phillips, *Phys. Plasmas* **8**, 606 (2001).
27. D. G. Hicks, C. K. Li, F. H. Séguin, A. K. Ram, J. A. Frenje, R. D. Petrasso, J. M. Soures, V. Yu. Glebov, D. D. Meyerhofer, S. Roberts, C. Sorce, C. Stöckl, T. C. Sangster, and T. W. Phillips, *Phys. Plasmas* **7**, 5106 (2000).
28. C. K. Li, F. H. Séguin, J. R. Rygg, J. A. Frenje, R. D. Petrasso, T. C. Sangster, V. A. Smalyuk, J. A. Delettrez, J. P. Knauer, S. P. Regan, J. Soures, F. J. Marshall, P. W. McKenty, D. D. Meyerhofer, C. Stoeckl, R. P. J. Town, P. Patel, A. J. MacKinnion, P. Amendt, N. Izumi, and O. Landen, *Bull. Am. Phys. Soc.* **50**, 266 (2005).
29. J. A. Frenje, C. K. Li, F. H. Séguin, J. Deciantis, S. Kurebayashi, J. R. Rygg, R. D. Petrasso, J. Delettrez, V. Yu. Glebov, C. Stoeckl, F. J. Marshall, D. D. Meyerhofer, T. C. Sangster, V. A. Smalyuk, and J. M. Soures, *Phys. Plasmas* **11**, 2798 (2003).
30. V. Yu. Glebov, C. Stoeckl, S. Roberts, T. C. Sangster, J. A. Frenje, R. D. Petrasso, R. A. Lerche, and R. L. Griffith, "Proton Temporal Diagnostics for ICF Experiments on OMEGA," submitted to Review of Scientific Instruments.